Predictions of radiation pattern and in-out asymmetries in the DEMO scrape-off layer using fluid neutrals

PAPER • OPEN ACCESS

Predictions of radiation pattern and in–out asymmetries in the DEMO scrape-off layer using fluid neutrals

To cite this article: L. Aho-Mantila *et al* 2022 *Nucl. Fusion* **62** 056015

OPEN ACCESS
IOP Publishing | International Atomic Energy Agency Nuclear Fusion
Nucl. Fusion **62** (2022) 056015 (12pp) https://doi.org/10.1088/1741-4326/ac4d62

Predictions of radiation pattern and in–out asymmetries in the DEMO scrape-off layer using fluid neutrals

L. Aho-Mantila[1,*], F. Subba[2], M. Bernert[3], D.P. Coster[3], S. Wiesen[4], M. Wischmeier[3], X. Bonnin[5], S. Brezinsek[4], P. David[3], F. Militello[6], The ASDEX Upgrade Team[a] and The EUROfusion MST1 Team[b]

[1] VTT Technical Research Centre of Finland, PO Box 1000, FI-02044 VTT, Finland
[2] NEMO Group, Politecnico di Torino, Corso Duca degli Abruzzi 24, 10129, Torino, Italy
[3] Max-Planck Institut für Plasmaphysik, D-85748 Garching, Germany
[4] Forschungszentum Jülich Gmbh, Institut für Energie- und Klimaforschung-Plasmaphysik, 52425 Jülich, Germany
[5] ITER Organization, Route de Vinon-sur-Verdon, CS 90046, 13067 St. Paul-lez-Durance Cedex, France
[6] CCFE-UKAEA, Culham Science Centre, Abingdon, OX14 3DB, United Kingdom

E-mail: leena.aho-mantila@vtt.fi

Received 6 September 2021, revised 6 November 2021
Accepted for publication 20 January 2022
Published 2 March 2022

Abstract

Strongly radiating and detached high-power discharges in present-day full-metal tokamaks have a characteristic radiation pattern involving condensation of radiation near the X-point, with significant radiative losses above the X-point. In contrast, Demonstration Fusion Power Plant (DEMO) divertor exhaust scoping studies using reduced physics models, including a fluid description for the neutrals, place the strongest radiation fronts in the divertor legs, near the separatrix. The present contribution studies sensitivity of the radiation pattern corresponding to maximal divertor impurity radiation to those physics models that are typically neglected in the simulations due to their computational expense: cross-field drifts, complex impurity models and kinetic neutrals. Model benchmarking is carried out in comparison to L-mode discharges, which are shown to feature both divertor and X-point radiation. The simulated plasma conditions with maximal divertor radiation have in–out asymmetries in the divertor legs and at the divertor entrance, and the asymmetries and the radiation patterns are observed to be sensitive to both cross-field drift effects and the neutral model. DEMO simulations, carried out using SOLPS-ITER, show an impact of cross-field drifts on the divertor asymmetries, but the impact is not large enough to move the radiation front from the divertor legs to regions above the X-point.

* Author to whom any correspondence should be addressed.

[a] See Meyer *et al* 2019 (https://doi.org/10.1088/1741-4326/ab18b8) for the ASDEX Upgrade Team.

[b] See Labit *et al* 2019 (https://doi.org/10.1088/1741-4326/ab2211) for the EUROfusion MST1 Team.

Keywords: DEMO, impurity radiation, SOLPS-ITER, in–out asymmetries, divertor physics, cross-field drifts, power exhaust

(Some figures may appear in colour only in the online journal)

1. Introduction

Scoping the possible operational regimes of a Demonstration Fusion Power Plant (DEMO) requires reliable models of power exhaust processes. In the European DEMO design, which is based on modest extrapolations from ITER [1], the scrape-off layer (SOL) and divertor will need a higher radiated power fraction than present-day tokamak devices. Strong asymmetries in the SOL and divertor conditions may reduce the operational window in which the targets can be protected from excessive power loading. DEMO predictions will need to couple the transport of plasma particles and dissipation of plasma power in the SOL with the various collisional processes and reactions involving neutrals in the divertor, which in practice requires using 2D plasma fluid codes. To overcome the long convergence times, which present a bottleneck for the predictions, various simplifications are applied to the physics models used in the codes [2, 3]. The possible reductions in the physics models include using a fluid model for the neutrals instead of a kinetic model, bundling the charge states of the impurities, and neglecting the effects of cross-field drifts [3]. Both cross-field drifts and kinetic neutrals have been shown in past benchmarking efforts to be important for reproducing various divertor regimes in present-day devices [4–8], but their importance for DEMO divertor conditions is largely unknown. Kinetic neutrals increase the credibility of modelling divertor detachment, pumping and radiation due to the fuel neutrals, but for modelling impurity radiation and the SOL power fluxes that enter the divertor legs, the drifts and the level of detail included in the impurity models could be equally or even more significant.

To stay below the erosion and power handling limits of the plasma-facing components, detached divertor conditions will be required in DEMO. In recent years, several experiments have been carried out in full-metal devices with DEMO-relevant divertor geometry to characterize impurity-seeded discharges, in which the strong impurity radiation can be considered as an essential ingredient in obtaining partial detachment, in which the heat fluxes and pressure are significantly reduced in the near vicinity of the strike point, or even complete detachment, which extends over the entire divertor target [9–15]. When light impurities like N_2 or Ne are used as the seeding gas, the radiation pattern evolves at low seeding levels asymmetrically between the two divertor legs, and at high seeding levels a condensation of radiation near and above the X-point is obtained, known in H-mode discharges as the X-point radiator (XPR) [15]. Heavier impurities like Ar, Kr and Xe tend to radiate more on closed flux surfaces, where at least Kr has been observed to yield a strong radiating ring in the pedestal region inside the separatrix [14]. Both the XPR and the radiating ring in the pedestal lead to a reduction in the power crossing the separatrix, P_{sep}, which facilitates detachment at the targets. In the case of dominant divertor radiation, strong temperature gradients are established near the X-point or further down in the divertor legs with smaller impact on P_{sep} and upstream pressure. As the ionization, transport and radiative efficiency of the impurities have strong dependence on the plasma conditions, particularly on the electron temperature, the characteristic radiation patterns may differ significantly between a DEMO reactor and present-day machines. Such qualitative differences and their impact on the parametric dependencies need to be taken into account when building predictions and extrapolation models.

Reduced physics modelling, like e.g. the fluid neutral treatment mentioned above, may offer a feasible way to address qualitative differences in the DEMO exhaust in comparison to present-day devices. In this paper we study the applicability of the reduced physics simulations to model the radiation pattern in DEMO edge plasmas corresponding to detached target conditions. Both the set-up of the simulations and the acceptance criteria of the edge solutions are kept similar to what has been used in recent DEMO scoping studies [16, 17], to understand the possibilities and limitations of fluid simulations for performing fast parametric studies. Section 2 describes the properties of the reduced physics solutions and compares these with results obtained with either activated drift terms, kinetic neutral treatment (referring to studies presented elsewhere), or using a different impurity model. In section 3, we discuss N_2-seeded L-mode experiments in ASDEX Upgrade and JET, which have been carried out to enable validation of simulations against DEMO-relevant radiative divertor conditions. We study the code solutions obtained for these experiments and present the effects of varying the physics description in the respective JET simulations. Conclusions from our studies are presented and discussed in section 4.

2. Predictions of divertor power exhaust in DEMO

Exhaust modelling studies on the European DEMO are concentrated on detailed modelling of the single-null (SN) configuration [2, 18, 19] as well as on comparative assessments of possible alternative divertor configurations (ADCs) [16, 17, 20–22]. We have taken the setup of the latter [21] as the basis of our simulation studies presented here, which use the SOLPS-ITER code package and, by default, a reduced physics model with bundled impurities [23], fluid neutrals and no drifts. All DEMO solutions studied in this paper correspond to the European SN DEMO-1 configuration using

the 2018 variant derived for the ADC studies as presented in [16, 21].

In the basic setup, it is assumed that 150 MW of the heating power enters through the core boundary of the simulation domain, which is only 50% of the power assumed to arrive to the pedestal region in DEMO. We call this the input power, P_{in}, to differentiate it from the heating power, $P_{\mathrm{heat}} = 300$ MW [16]. This is a simplification made to reduce the computational effort required to scope power exhaust in the divertor and SOL regions; the implicit assumption is that the high-Z radiators, foreseen to be Kr or Xe, will radiate primarily on closed flux surfaces in the main chamber, and the impact on the divertor conditions can be accounted for by simply reducing the power fluxes crossing the separatrix, without explicitly including these radiators in the simulations. From PROCESS [16] calculations, the core/pedestal radiation is estimated to be 150 MW, which means that the power load challenge can be described with the parameter P_{sep}/R having a value of 16.7 (P_{sep} being just above the H-mode threshold level 110–135 MW for ion $\mathbf{B} \times \nabla \mathbf{B}$ drift pointing downwards into the divertor [16, 24]). For the divertor radiation, it is assumed that the differences in radiation characteristics of the low-Z impurities (N, Ne, Ar) are not large and the influence of design choices (e.g. divertor geometry) can be studied by simulating only one seeded impurity, in our case Ar.

The fuel is simplified to consist of only D, and He is the only intrinsic impurity included in the calculations. Erosion of W from the plasma-facing components is not taken into account, as the attached solutions do not aim to represent true operating conditions, but are shown to explain the dependence of Ar radiation and drift effects on the divertor conditions. W is also not included in the simulations of JET and AUG plasmas discussed in section 3, as the possible small level of core radiation due to W is taken into account when fitting the input parameters upstream, and the erosion yields in the divertor are low [25]. Fuelling is specified as a fixed D ion flux $\Gamma_{\mathrm{D}} = 3.5 \times 10^{22}$ s^{-1} through the core boundary to mimic pellets and, additionally, as a variable gas puff distributed along the SOL (north) boundary of the simulation grid to control the upstream density level. Pumping is described by a leakage of neutrals through the private flux boundary of the simulation grid (1% of the local neutral sound-speed flux, $n_{\alpha} c_{\mathrm{s},\alpha}$). The leakage level may influence the required D puffing level to reach a requested upstream density level, as well as the required impurity seeding level to reach a desired radiation level. The seeding is specified only through the SOL boundary (neutral Ar), although in earlier studies also core boundary conditions for the Ar density have been used [20].

The requirements for power mitigation can be expected to depend on the SOL width, which is characterized by the power decay length, λ_{q}. We assume that there is no poloidal variation in the cross-field transport. When also no dependence on puffing or seeding levels is assumed for the transport coefficients, λ_{q} is observed to vary depending on the plasma conditions. The low values of heat and particle diffusion (0.1–0.3 m^2 s^{-1}) specified as in [17] yield λ_{q} largely in the range of projections made from present-day devices to DEMO (1–5 mm [16, 26]).

The operational space has been defined in recent studies by the following criteria [17]: the outer midplane separatrix density is limited to $n_{\mathrm{sep}} < 0.6 n_{\mathrm{GW}}$, where n_{GW} is the Greenwald density, to allow for good plasma confinement. The extrapolation of the density limit, at which the confinement begins to reduce, is not yet thoroughly understood, therefore a fraction of n_{GW} not much larger than that observed in H-mode plasmas in ASDEX Upgrade and JET ($n_{\mathrm{sep}} < 0.4$–$0.5 n_{\mathrm{GW}}$) is chosen as the limit, the level being reduced in comparison to earlier modelling studies ($0.7 n_{\mathrm{GW}}$ was used in [2]). At the targets, the maximum electron temperature, $T_{\mathrm{e,t}}^{\mathrm{max}}$, should be less than 5 eV to avoid excessive W sputtering by the low-Z impurities that are abundant in the divertor [16], and the perpendicular heat flux to the target should be kept below 10 MW m^{-2} to ensure sufficient heat removal assuming an axisymmetric target (3D effects may result in higher local peak heat fluxes). In the present paper, only the evolution of the peak target temperature is studied in detail. The detached cases presented in the 2D plots all have $T_{\mathrm{e,t}}^{\mathrm{max}} < 2$ eV, at which level the power loads have not been observed to exceed the specified limit [19, 21, 22].

2.1. Power exhaust characteristics in reduced physics simulations

Figure 1 shows, in (a), the computational grid coloured by specific regions, and (b), the evolution of the radiation pattern, and (c), the evolution of the target conditions when the impurity seeding is gradually increased and the DEMO solution with the basic, reduced physics setup evolves into the operating space. These results are obtained at a constant upstream density, $n_{\mathrm{sep}} = 4.0 \times 10^{19}$ m^{-3} ($0.57 n_{\mathrm{GW}}$). The evolution of the radiation pattern is observed to follow similar trends as present-day experiments: radiation increases first in the inner divertor, which also detaches first, followed by a radiation increase in the outer divertor at higher seeding levels. Maximum radiated power is obtained as both divertor legs have approximately equally strong radiation level, and this coincides with the cooling of the outer target to $T_{\mathrm{e,t}}^{\mathrm{max}} < 5$ eV. The outer target ion fluxes are observed to drop as the seeding level is further increased, with a simultaneous saturation of the radiated power fraction in the SOL and divertor, f_{rad}, which is defined here as the modelled total radiated power divided by the input power used in the simulation (thus including also a small fraction of radiation modelled for the closed field line region). Further increase of the seeding level leads to an increase in core radiated power and a simultaneous decrease of the divertor radiated power. Despite the deep detachment of the outer divertor plasma, characterized in figure 1(*c*) by a drop in the total ion fluxes by a factor of 100 and cooling of $T_{\mathrm{e,t}}^{\mathrm{max}}$ to 0.6 eV, the strongest Ar radiation front stays in the divertor and does not move to closed field lines, and f_{rad} does not increase much above 70%. Note that f_{rad} defined here is smaller than a radiated power fraction calculated over the whole plasma region which, depending on the definition, includes also 150-300 MW of radiation losses on closed field lines due to line radiation, synchrotron radiation and Bremmstrahlung.

The radiation patterns corresponding to the different levels of Ar seeding are shown in figure 2. In figure 2(*a*), the outer

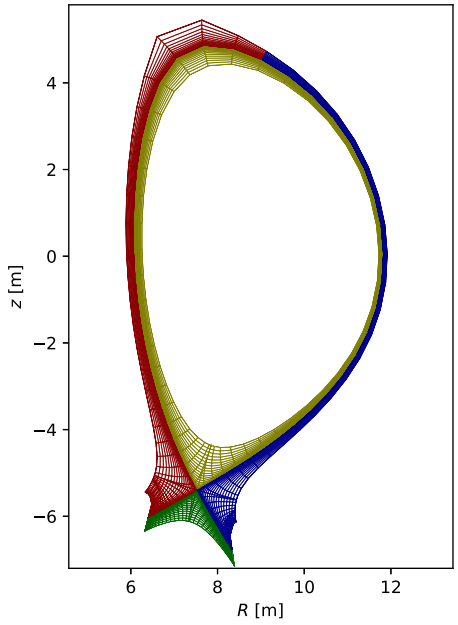

(a) SN computational grid, with various regions highlighted.

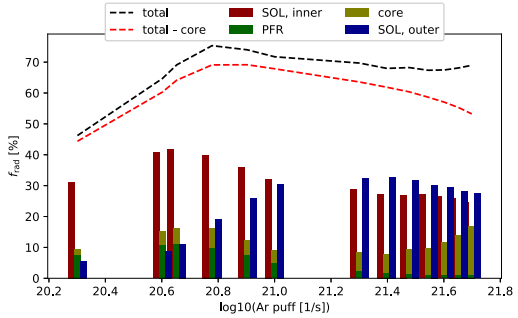

(b) Modelled radiated power fractions in the different regions of the plasma shown in Figure 1a (defined as power radiated in that region divided by P_{in}).

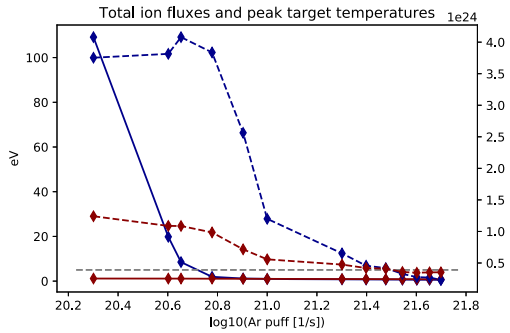

(c) Modelled integrated ion fluxes (dashed lines) and peak electron temperatures (solid lines) at the two divertor targets. The colour coding is as in Figure 1b: red for the inner target and blue for the outer target. The ion fluxes at the outer target begin to reduce as the peak electron temperature drops below 5 eV.

Figure 1. Evolution of the radiation pattern and target conditions in the DEMO SN configuration, modelled using the reduced physics setup. The upstream density is kept fixed at $n_{\mathrm{sep}} = 4.0 \times 10^{19}$ m^{-3} and the Ar puffing level is varied.

target is still attached and the radiation front is primarily in the inner divertor leg, whereas in figure 2(*b*) the outer target has just detached and strong radiation is obtained near both target plates. In figure 2(*c*), the strongest level of Ar seeding is used and the radiation front has moved away from the targets, closer to (but not to the direct vicinity or above) the X-point. The divertor temperature distribution corresponding to the strongest Ar puffing rate (5.0×10^{21} at/s) is also shown in figure 2. The temperature in the cells directly above the X-point is above 170 eV on the closed field lines and above 130 eV on the open field lines right next to the separatrix. Below the X-point, there is a strong temperature gradient and T_{e} is reduced to ~ 3 eV in the cells directly below the X-point, in the private flux region.

Cases with lower upstream density yield similar radiation patterns and radiated power fractions. A scan of operating points corresponding to different levels of D and Ar puffing ($n_{\mathrm{sep}} = 2.5$–3.9×10^{19} m^{-3}) was shown in figure 8 in [21], and the radiated power fraction on open field lines in all of the detached cases varied between 65% and 80%. The fraction of power radiated on closed field lines was observed to increase with reducing upstream density, reflecting the fact that more Ar needs to be puffed to obtain detached conditions at lower densities. However, also in all of these cases, no significant X-point radiation was observed, but the strongest radiation fronts were obtained along the divertor legs.

2.2. Role of the simplified physics models

As a first improvement of the physics model, we have investigated the role of cross-field drifts. Figure 3 shows a comparison between the reference Ar seeding scan and a similar scan with full drift effects included at the same upstream density level, $n_{\mathrm{sep}} = 4.0 \times 10^{19}$ m^{-3}. As in present-day devices, activation of cross-field drifts increases the peak outer target temperature in DEMO, when the directions of the magnetic field and plasma current are assumed to be similar to ITER (ion $\mathbf{B} \times \nabla \mathbf{B}$ drift points downwards into the divertor, co-directed current). To cool down the target to acceptable level, a higher Ar seeding level is needed in the simulations compared to simulations without drifts. This increases the Ar concentration, c_{Ar}, and the radiated power fraction required to obtain $T_{\mathrm{e,out}}^{\mathrm{max}} < 5$ eV, as shown in figure 3. The radiation increase is observed primarily in the inner divertor, in which higher densities and broader distribution of the power fluxes is obtained in the radial direction (also typical for drift effects in present-day devices). The in–out asymmetry is largest when the outer divertor is still attached and reduces, but does not vanish, for the detached solutions.

Figure 4 shows the same SN case as discussed in figure 2(*b*), but with cross-field drifts activated and Ar seeding level readjusted to obtain detached conditions at the targets. The radiation pattern is largely similar to that shown in figure 2(*b*), and there is no significant radiation in the SOL regions close to the X-point. The largest difference is in f_{rad}, which increases to a level close to 80%, being higher than in the solution without drifts. Although a full matrix scan (Γ_{D}, Γ_{Ar}) of the solutions with drifts included is not yet available, the results indicate a reduction rather than an increase of possible operating points (in terms of the range of possible combinations of upstream densities and impurity concentrations) with the activation of drift terms, due to the higher levels of c_{Ar} required with drifts.

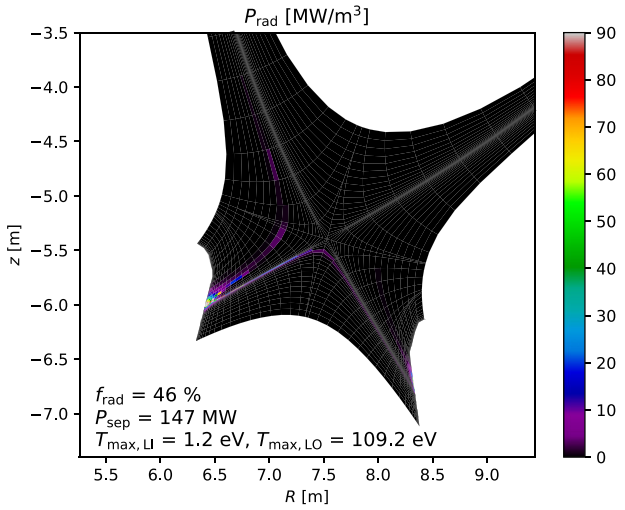

(a) Radiation pattern, $\Gamma_{\mathrm{Ar}} = 0.2\mathrm{E}21\ \mathrm{s}^{-1}$.

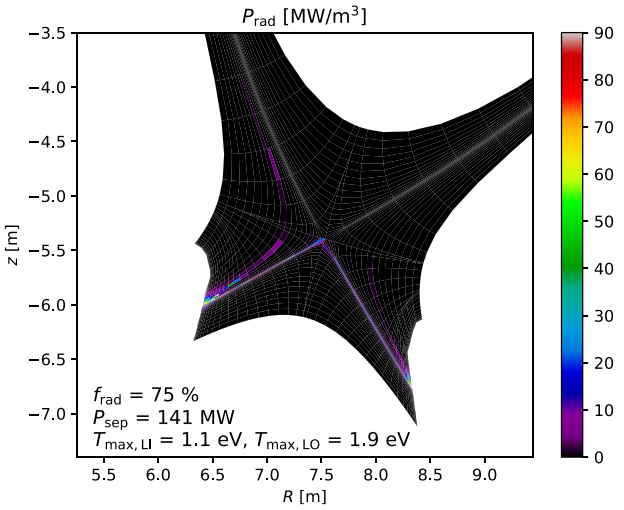

(b) Radiation pattern, $\Gamma_{\mathrm{Ar}} = 0.6\mathrm{E}21\ \mathrm{s}^{-1}$.

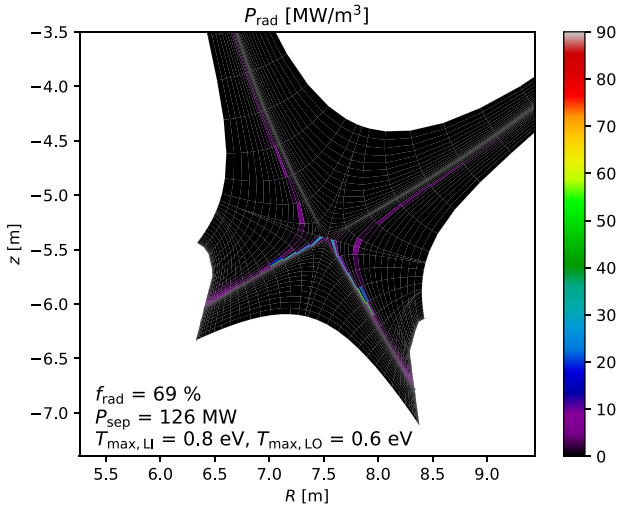

(c) Radiation pattern, $\Gamma_{\mathrm{Ar}} = 5\mathrm{E}21\ \mathrm{s}^{-1}$.

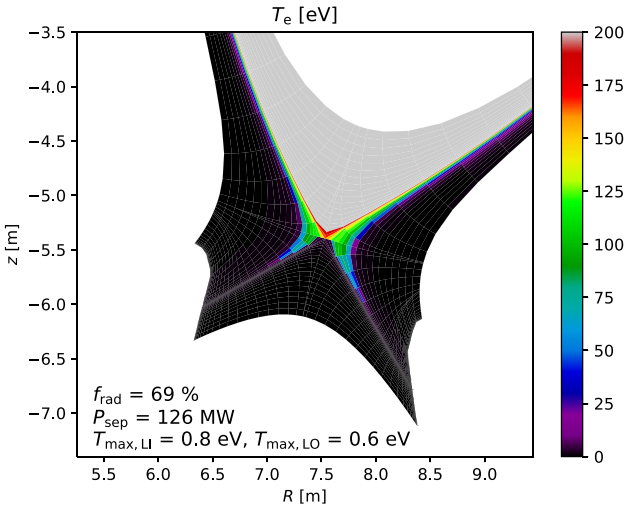

(d) Temperature distribution, $\Gamma_{\mathrm{Ar}} = 5\mathrm{E}21\ \mathrm{s}^{-1}$. Regions with $T_e > 200$ eV are not included in the picture.

Figure 2. Divertor radiation ((*a*)–(*c*) panels) and temperature (*d*) in the SN reference case. The extent of the full computational mesh is shown in figure 1(*a*). $T_{\mathrm{max,LI}}$ and $T_{\mathrm{max,LO}}$ refer to the maximum electron temperatures at the lower inner target and lower outer target, respectively.

The role of neutrals for the radiation pattern can be derived from figure 5, which shows the D ionization pattern in the fluid neutral [27] simulation case of deepest detachment shown in figure 2(*c*). The ionization fronts are located close to the radiation fronts, and the neutral densities and all processes related to the neutrals, e.g. CX reactions, reduce rapidly when moving across these ionization zones towards the closed field lines. On the SOL flux ring directly outboard the separatrix, the maximum D neutral concentration is only 0.03%, although increasing to 10 times this level in the cells directly below the X-point. The neutrals radiate less than 10% of P_{in}, and most of this radiation comes from regions outside of the ionization zones, closer to the targets. Recombination is also strongest in the region between the ionization fronts and the targets, as expected. Despite the strong cooling of the divertor legs, high level of radiation, and relatively low level of P_{sep}, the direct impact of neutrals to the conditions in the region immediately surrounding the X-point is minimal.

The radiation pattern is seen to remain largely similar when moving to fully kinetic neutral simulations [19], with simulation parameters otherwise close to the simplified case studied here. The strongest radiation fronts are along the divertor legs, and the high temperatures at the divertor entrance prevent the neutrals from having a significant contribution to the conditions at the X-point or on closed field lines. It seems therefore unlikely, that the neutral model would play a large direct role in the radiation pattern on either closed field lines, at the X-point, or in the divertor legs (this last region confirmed in [19]) in DEMO. Similar to drifts, indirect effects may be possible with an improved neutral model, if the required impurity radiation levels for detachment change. According to [19], however, the change in f_{rad} is not large but at most of the same order as observed with the activation of drifts. Effects of including more advanced physics models, like the recently discussed CX reactions between the fuel and the impurity ions [28], will need to be studied separately in the future.

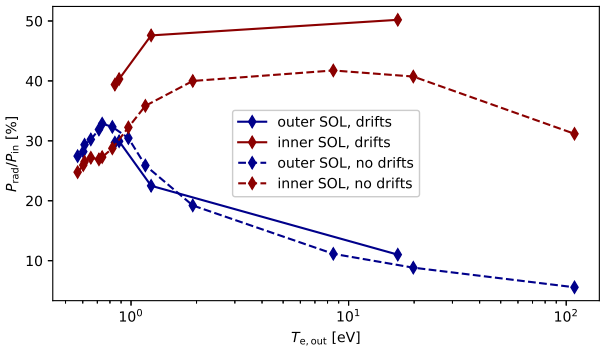

(a) Radiated power fractions on the inner and outer sides of the SOL, defined as in Figure 1b.

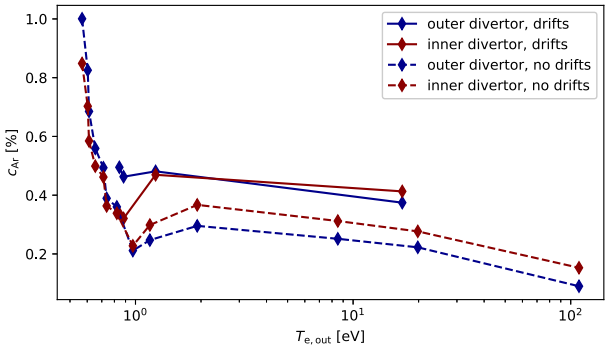

(b) Ar concentrations in the divertor legs, calculated as an average value on the computational cells below the X-point, which are in the SOL within 3 power decay lengths from the separatrix.

Figure 3. Radiated power fractions and Ar concentrations as a function of the peak electron temperature along the outer target. Results with activated drift terms are drawn with the solid lines, results without drifts are drawn with the dashed lines.

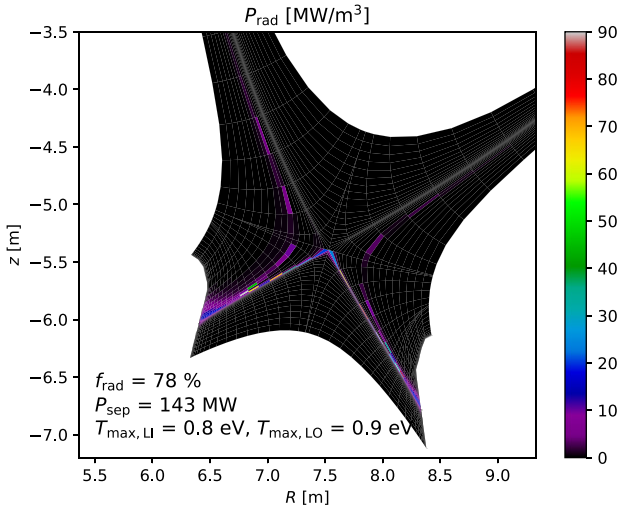

Figure 4. Radiation pattern, $\Gamma_{Ar} = 2.3 \times 10^{21}$ s^{-1}, drifts activated.

The choice of the seeding impurity impacts the radiation distribution in the divertor and SOL, due to the differing efficiency of each impurity species to radiate at a given background plasma temperature, and the resulting differences in the local cooling of the plasma. Heavier impurities will also travel

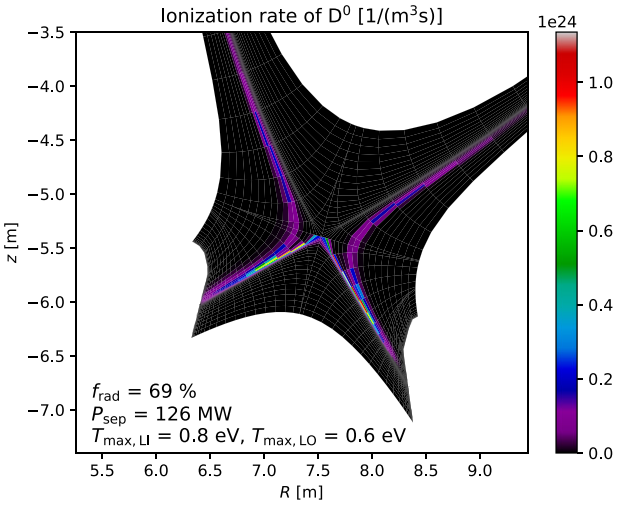

Figure 5. D ionization pattern, $\Gamma_{Ar} = 5 \times 10^{21}$ s^{-1}, no drifts.

further towards the core plasma before being fully ionized. In present-day devices, both N and Ne have been observed to create divertor and X-point radiation when injected at high levels. The steady-state radiation patterns of the higher-Z impurities Ar, Kr, and Xe, are not as well-characterized, but they are associated with a larger radiated fraction at the pedestal, and in some cases a poloidally radiating ring is formed at this location. In DEMO, the lighter impurities N, Ne and Ar all are modelled to radiate primarily in the divertor, although the fraction of radiation on closed field lines increases when the upstream density is reduced [21] or when P_{sep} is reduced [2]. De-bundling of the Ar impurities does not have a significant effect on the radiation pattern.

An attempt was made to use the reduced physics model to simulate higher-Z impurities, which are expected to radiate more in the pedestal relative to the divertor. For this purpose, the input power was raised to almost the full 300 MW expected to arrive to the pedestal region ($P_{in} = 260$ MW), and Xe impurities were added to the solution in a similar way as Ar, with simultaneous seeding of both impurities. In the few cases that converged within our limited investigations (comprising several dozen cases with varying impurity levels), Xe was found to radiate almost exactly in the same regions as Ar, see figure 6(*b*). Together with a strong Ar seeding rate, the solutions allow for $P_{sep} = 230$ MW with detached divertor conditions, although the small level of pedestal radiation was not a goal of our study. Notably, in all of our detached solutions, $\sim$15% of the input power is lost through the north boundary as ion/neutral heat flux, so that less power reaches the divertor entrance. The maximum temperature at the divertor entrance is above 200 eV, at which level the radiation efficiency of both species is reduced. It is possible that with a different seeding location, higher Xe radiation would be obtained in the closed field line region [18]. Furthermore, the bundled impurity description may play a more important role in the case of the heavy impurity Xe but, due to the large number of charge states involved, de-bundling in this scenario was left for future investigations.

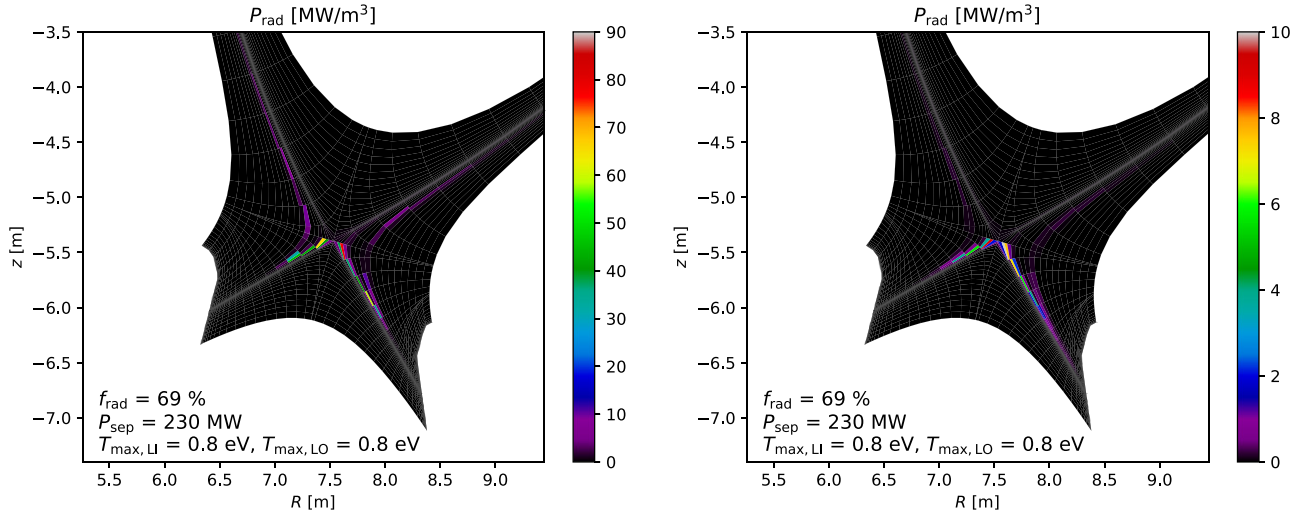

(a) Ar radiation pattern.

(b) Xe radiation pattern (note the different scale).

Figure 6. Simulated radiation patterns of extrinsic impurities, when both Ar and Xe are seeded simultaneously: $P_{in} = 260$ MW, $n_{sep} = 3.7 \times 10^{19}$ m^{-3}, $\Gamma_{Ar} = 1 \times 10^{22}$ s^{-1} and $\Gamma_{Xe} = 3 \times 10^{20}$ s^{-1}.

3. Benchmarking of the reduced physics models against L-mode experiments

The influence of the various physics models is further studied in comparison to present-day experiments. For this purpose, experiments featuring strong in–out asymmetries and impurity seeding to cool down both targets are discussed. To avoid additional physics ingredients arising from ELMs, confinement changes, strong fluctuations, or significant W radiation, the studies focus on a series of well-diagnosed L-mode discharges carried out in ASDEX Upgrade and JET, part of which have been extensively studied in past code-experiment validation works. Details of the transport barrier are expected to have a smaller impact on the results discussed in the present work than processes taking place in the divertor and in the SOL, justifying the use of low-confinement mode plasmas for model benchmarking. Furthermore, the low density used in the studied discharges reduces the collisionality of the plasma at the divertor entrance, leading to stronger gradients in the divertor compared to discharges with higher density, which makes our studies more relevant in view of DEMO. In section 3.1, we describe the radiative regimes obtained in these experiments, while in section 3.2 application of reduced physics modelling is demonstrated.

3.1. Radiative regimes in low-density L-mode experiments

Unseeded low-density L-mode plasmas in the full-metal devices ASDEX Upgrade and JET have been described in [5, 6]. When the ion $\mathbf{B} \times \nabla\mathbf{B}$ drift is pointing downwards in a lower-SN configuration, the outer divertor is typically in a low-recycling regime, whereas the conditions in the inner divertor may vary from detached to high-recycling depending on the machine, divertor and magnetic geometry, and the exact density level used in the experiment. The in–out asymmetry has been shown to be influenced by a combination of poloidal and radial drifts and further enhanced by thermoelectric currents in these machines [6, 30, 31]. When N is seeded into these plasmas, but the upstream conditions are kept unchanged via feedback control on the line-averaged density, radiation is first observed to increase in the cooler inner divertor, and at higher seeding levels in the outer divertor [29, 32]. Figure 7 shows radiated power fractions, defined as $f_{rad} = P_{rad}/P_{heat}$ in the total plasma volume, obtained in the two very similar L-mode experiments carried out in ASDEX Upgrade and JET. In the unseeded discharges, both devices have low-recycling conditions and maximum target temperature over 30 eV in the outer divertor. Maximum divertor radiation level and a total $f_{rad} \sim 60\%$ is obtained when the radiation front extends over both divertor legs, similar to the DEMO predictions. Increasing the impurity seeding level further leads to a reduction in the integrated ion fluxes at both targets [29], which is also consistent with the DEMO simulations.

Existence of an X-point radiating regime in L-mode has not been thoroughly investigated in the past. For this purpose, we discuss previously unpublished results from a series of N-seeded discharges carried out at ASDEX Upgrade to complement the above observations at higher levels of f_{rad}. The toroidal magnetic field was kept unchanged (2.5 T) with respect to the earlier experiment series discussed in figure 7(*a*), but the plasma current was reduced to 0.8 MA (compared to 1.0 MA). Normal field direction (ion $\mathbf{B} \times \nabla\mathbf{B}$ drift pointing downwards into the divertor) was used. In figure 8, time traces of some of the most representative discharges in this series are shown.

In the unseeded reference discharge, #30286, and in the first discharge with N-seeding, #30287, the line-averaged density (H-1) is kept at 3.8×10^{19} m^{-3} by a feedback D gas puff, and 0.2 MW ECRH heating is used. N-seeding applied at a constant rate of 2×10^{21} s^{-1} leads to a modest increase in radiation, and the radiation front is mainly in the divertor. The T_{div} signal, which is the main signal used to indicate changes in the detachment level [10], is reduced from 10 eV to 2 eV. The conditions

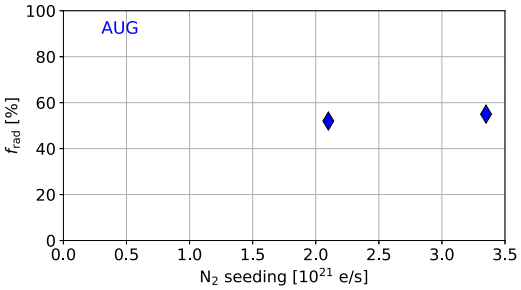

(a) Radiated power fractions from 2D tomography in ASDEX Upgrade discharges #28818 and #28795 (discharge #28818 has been described in [6]; main difference between #28795 and #28818 is the N seeding level). The radiated power level in the unseeded reference discharge #27691 was too low for reliable f_{rad} calculation. Higher seeding levels led to disruptions.

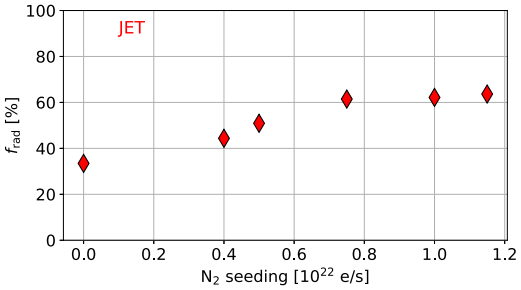

(b) Radiated power fractions in JET discharges #82291-#82299. The data is taken from [29].

Figure 7. Radiated power fractions in ASDEX Upgrade and JET N-seeded L-mode discharges at low density.

resemble the conditions of the earlier experiment discussed in figure 7(*a*).

A higher N-seeding level applied in #30800 leads at 2.1 s to a sudden drop of T_{div} to values below 1 eV, and a simultaneous increase in the radiated power is observed. At this moment, a transition in the radiative regime from divertor-dominated radiation to X-point radiation (more precisely, radiation above the X-point) is observed, see figure 9(*b*). The regime is not stable, as the radiation front continues to move upwards in the confined plasma region, and the discharge ends with a disruption at 3.4 s.

In the following two discharges, #30801 and #30802, the ECRH power was increased to either 0.9 MW (#30801) or to 1.5 MW (#30802) at 2.5 s, shortly after the transition to the X-point radiating phase. The radiation front, which is observed to move upwards above the X-point in the period of 2.1 s to 2.5 s, moves back down towards the X-point at 2.5 s when the higher heating power is applied, see figure 9(*c*). The total radiated power also increases significantly as more plasma power arrives to the radiating zone, and $f_{\mathrm{rad}} \sim 90\%$ is estimated based on simplified tomography of the bolometer measurements [33]. The radiation front is not completely stable, but the evolution is significantly slower compared to the lower heating power and the discharge ends as planned. Increase in the line-averaged density is observed first at the on-set of the X-point radiating phase and later with the application of the stronger ECRH power. These two stepwise increases are likely due to changes in the fuelling efficiency caused by the modified conditions near the X-point. In discharge #30802, a further stepwise increase in the density is observed at 2.8 s together with the appearance of ELMs, indicating a change in the confinement regime to H-mode.

The details of the discharges likely deserve a separate study, but from the point of view of the present study, the important information is that the physics mechanisms responsible for the movement of the radiation front from the divertor to the regions above the X-point are present in L-mode, although less studied than in H-mode. The creation of the X-point radiative regime is, therefore, connected to the divertor conditions, and does not require such transport properties, which are specific to H-mode plasmas. The higher power fluxes are observed to stabilize the radiation on closed field lines in ASDEX Upgrade, but it is possible that larger devices with higher power levels always satisfy this condition, regardless of the confinement regime.

Comparing the DEMO predictions with these experimentally characterized radiative regimes, we see a close resemblance to the regime with radiation dominantly in the divertor, whereas the XPR is completely missing in our predictions for DEMO. This contradicts the regular observations of XPR in fully detached high-power discharges in the full-metal devices. As discussed above, a prerequisite for the XPR appears to be the strong radiation in the divertor at lower seeding levels, which modifies the local plasma conditions near the X-point and allows for the radiation front to move to closed field lines. Therefore, in the following we focus on the regime of strong divertor radiation when performing our model variations, to better understand the physics that is needed to accurately describe the divertor radiation, which forms the basis for the possible regime transition. Simulations including XPR are not presented here, but they have been discussed in [32] (L-mode) and [11, 34] (H-mode), with [34] providing the most advanced discussion on the associated numerical efforts.

3.2. Comparing complex and reduced physics simulations

A comparison between the reduced-physics simulations and more complex simulations is performed for the low-density L-mode radiative scenario described in figure 7. For this purpose, we use previously reported SOLPS5.0 simulations [6, 29, 32] of these experiments, which include all the main physics ingredients, which were available in the code package at that time. More specifically, cross-field drifts are activated, kinetic neutral model (Eirene) is used and all charge states of N are simulated. Although the code version is different from what was used in the DEMO predictions, the SOLPS5.0 simulations can be reduced to study the same physics ingredients as in the SOLPS-ITER simulations in section 2, the main difference being the N impurity species compared to Ar impurity species (for the differences in the numerical implementation of the drifts, see [35]). In figures 10(*a*)–(*f*), we show the modelled 2D distributions of divertor radiation, temperature and density in the solutions corresponding to the conditions, in which the divertor radiated power saturates. The conditions in the two devices are very similar: both show a significant

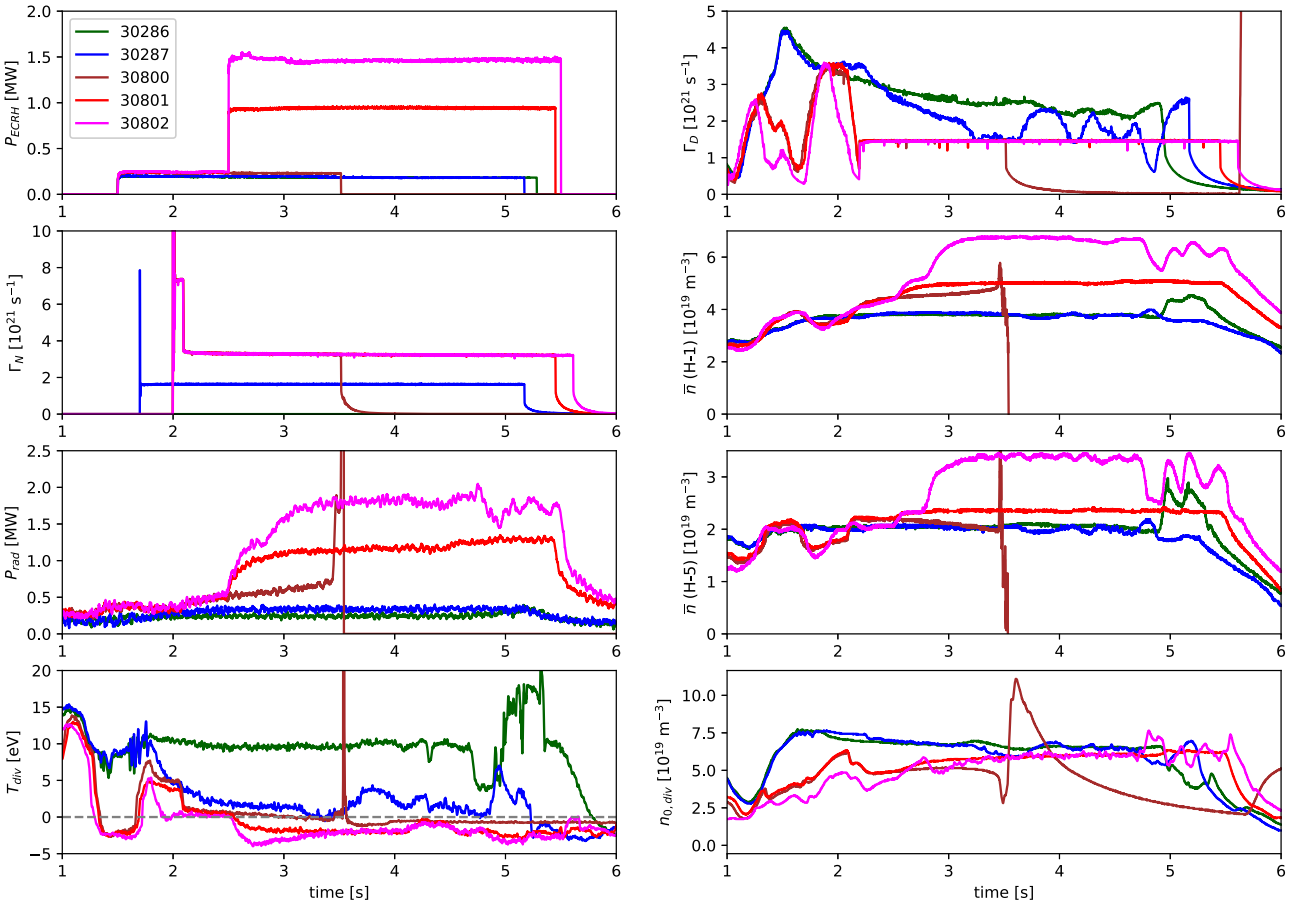

Figure 8. Time traces in the L-mode N-seeding experiments in ASDEX Upgrade. After 3.0 seconds, all discharges have diagnostic measurements involving variations in the plasma position, reciprocating probe plunges and neutral beam blips, which cause perturbation in some of the measured signals presented here. H-1 and H-5 refer to the core and edge locations, and the signal used for P_{rad} shows the qualitative evolution of total radiation with high time resolution, but the absolute value of the signal may not be accurate (f_{rad} evaluations in this paper are based on more reliable tomography).

cooling of the inner divertor leg, also in locations above the X-point, in which the cells adjacent to the separatrix have temperatures around 20–40 eV. The in–out asymmetry is visible in the density as well, and the highest densities are modelled for the inner divertor leg, also in regions close to the X-point. The strongest radiation is obtained in the near vicinity of the X-point and along the outer divertor leg.

The reduced physics SOLPS5.0 simulations corresponding to the setup used in the DEMO modelling, i.e. without cross-field drifts and using fluid neutrals and N impurities bundled into three charge groups, are shown in figures 10(g)–(i) for the JET plasma. The JET plasma is chosen for this model variation, as it may allow better for a regime transition, which could be observed at higher seeding levels when using the complex simulation set-up [32]. When using the reduced-physics setup, the impurity seeding level is re-adjusted to obtain outer target temperatures $\leqslant 5$ eV, but the required f_{rad} is observed to be very similar to the complex simulation. Although the results are visibly different from the results obtained with the complex simulation, some key similarities remain. The strong asymmetry in the plasma temperature between the two divertor legs is present also in the reduced physics simulations, and it is observed to have a large impact on the radiation pattern, which also is asymmetric. There is condensation of radiation close to the X-point in both divertor legs. The density asymmetry observed in the complex simulations is, however, not reproduced by the reduced physics simulations.

In figure 10(j)–(l), similar reduced physics simulation results are shown, with the exception that drift terms are fully activated. Activation of the drift terms is observed to yield a strong density asymmetry similar to the complex simulations. The drifts have a smaller role in the radiation pattern, which largely follows the temperature distribution. Both the temperature and the radiation asymmetry is larger in this case than in the complex simulation, but the difference is small. Particularly in regions close to the X-point, there is a good agreement between the reduced physics simulation with drifts activated and the complex simulation. The strongest radiation is obtained immediately next to the X-point, although not on closed field lines. The required radiated power fraction to cool down the targets varies depending on the physics included, and the highest f_{rad} is obtained in the reduced physics simulations with drifts activated.

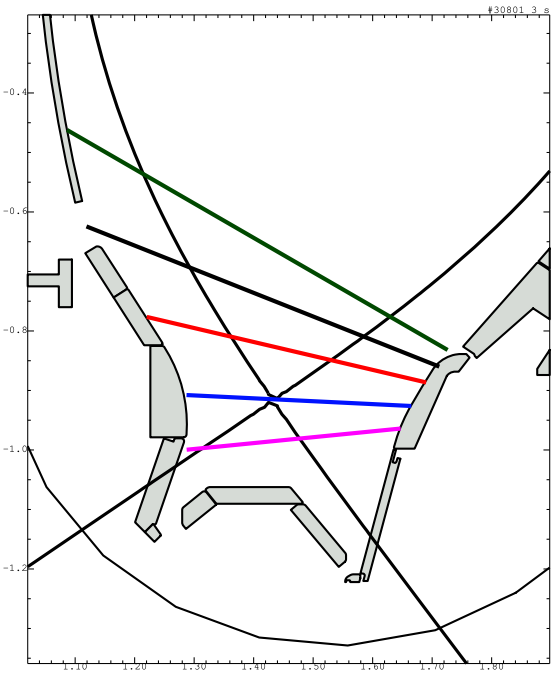

(a) Selected bolometer lines-of-sight in discharges #30800 and #30801. The colour coding is the same as in Figures (b) and (c).

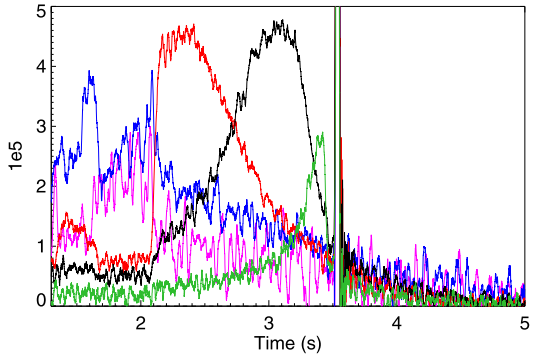

(b) Measured radiation (qualitative) in discharge #30800.

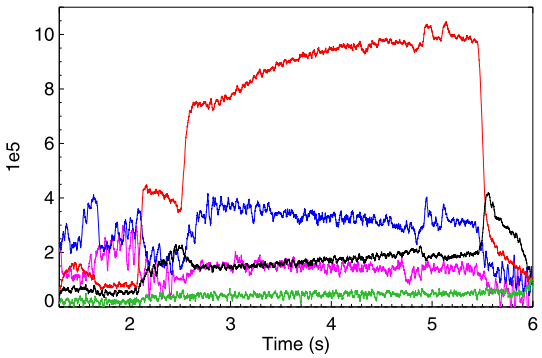

(c) Measured radiation (qualitative) in discharge #30801.

Figure 9. Movement of the radiation front in the disruptive discharge #30800 and in the more stable discharge #30801, in which stronger ECRH power is applied at 2.5 s. Change from divertor radiation to X-point radiation happens in both discharges at 2.1 s.

4. Discussion and conclusions

In the present contribution, we have focused on characterizing the divertor radiation pattern in DEMO using the SOLPS-ITER code, and investigated its sensitivity to the various physics ingredients, which typically are neglected when scoping studies are made. The inclusion of more detailed physics, such as the drifts studied in the present paper or the kinetic neutral model studied in [19], may alter the radiated power fraction, change the required impurity seeding levels to reach detachment and modify the in–out asymmetries in the DEMO-scale simulations. However, the primary regions in which the radiation is strongest are not significantly changed by any of these ingredients acting alone in the solutions. The presently predicted divertor radiation patterns in detached regime in DEMO include strong radiation along both divertor legs and no significant concentration of radiation near the X-point, when $P_{\mathrm{sep}} = 150$ MW is assumed. The radiation pattern is similar to those predicted for ITER using kinetic neutrals and activated drifts and $P_{\mathrm{sep}} = 100$ MW [36].

When similar model variations are performed in SOLPS5.0 simulations of present-day L-mode experiments with similar level of divertor radiation, larger variations in the modelled radiation pattern are observed. In–out asymmetries in the position of the radiation front relative to the X-point height appear stronger in the smaller devices than in DEMO, and asymmetries are observed even when using the reduced physics modelling, suggesting that geometry may play a significant role. Drifts have a larger role in modifying the divertor density asymmetry in these low-density, strongly seeded discharges, than the neutral and impurity models. Strong radiation in the SOL close to the X-point is obtained in both complex and reduced physics simulations.

From the results obtained one can conclude that it is important to include more detailed physics, like the drifts, when estimating absolute levels of particle and power fluxes reaching the DEMO divertor targets. Consequently, reduced physics modelling should be used with great caution if the purpose is to provide quantitative estimates of the operating space for a detailed engineering design. Further to this, uncertainties in the cross-field transport levels and the upstream density limit are a challenge for all predictions, which aim for quantitative results, and more studies are required in this area to strengthen our predictive capabilities in view of power exhaust in DEMO.

Reduced physics modelling can, however, help to identify qualitative features and guide future analyses of power exhaust in DEMO. An example of this is the persistently low level of radiation at the X-point height in our simulations, which does not appear to be an artefact of missing physics in the calculations, although combined effects of the possible physics improvements are not yet explored. It is possible that, with a carefully adjusted impurity source location, higher-Z

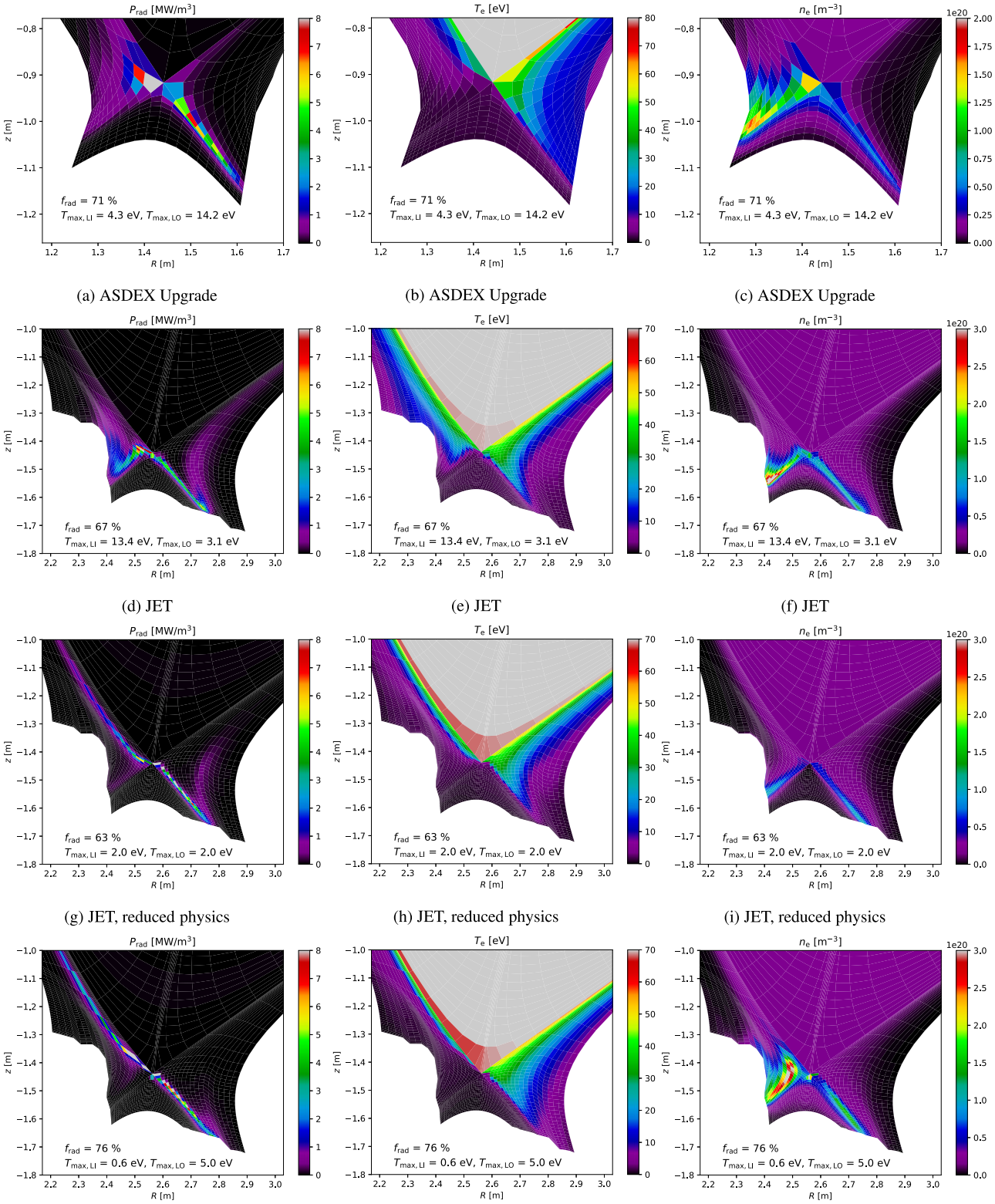

(a) ASDEX Upgrade (b) ASDEX Upgrade (c) ASDEX Upgrade

(d) JET (e) JET (f) JET

(g) JET, reduced physics (h) JET, reduced physics (i) JET, reduced physics

(j) JET, reduced physics + drifts (k) JET, reduced physics + drifts (l) JET, reduced physics + drifts

Figure 10. Radiation patterns in ASDEX Upgrade and JET simulations. On the two uppermost rows, results from simulations using complex physics models (drifts, kinetic neutrals, unbundled N impurities) are shown [32]. The bottom two rows show the effects of reducing the physics description.

impurities (Kr, Xe) needed to radiate the remaining 150 MW of P_{heat}, which was not accounted for in this work, will form an XPR. However, as long as $P_{sep} = 150$ MW, a significant radiation in the divertor legs can be expected by the lower-Z impurities (e.g. Ar) in this scenario as well, which differs from some of the highly radiating regimes encountered in present-day devices. Future work will be needed to address the role of high-Z impurities in DEMO as well as the possible deviations of P_{sep} from the presently used assumption of 150 MW.

Acknowledgments

The work has received funding from the Academy of Finland (Decision Number 289726). This work has been carried out within the framework of the EUROfusion Consortium and has received funding from the Euratom Research and Training Programme 2014–2018 and 2019–2020 under Grant Agreement No. 633053. The views and opinions expressed herein do not necessarily reflect those of the European Commission, of the Academy of Finland, or of the ITER Organization.

ORCID iDs

L. Aho-Mantila https://orcid.org/0000-0002-0587-9857
F. Subba https://orcid.org/0000-0002-8170-4792
D.P. Coster https://orcid.org/0000-0002-2470-9706
S. Wiesen https://orcid.org/0000-0002-3696-5475
S. Brezinsek https://orcid.org/0000-0002-7213-3326
P. David https://orcid.org/0000-0003-4837-8507
F. Militello https://orcid.org/0000-0002-8034-4756

References

[1] Federici G. *et al* 2019 *Nucl. Fusion* **59** 066013
[2] Subba F., Aho-Mantila L., Coster D.P., Maddaluno G., Nallo G.F., Sieglin B., Wenninger R. and Zanino R. 2018 *Plasma Phys. Control. Fusion* **60** 035013
[3] Coster D.P. Contrib. Plasma Phys. 56 790–795.
[4] Wischmeier M. *et al* 2009 *J. Nucl. Mater.* **390–391** 250–4
[5] Aho-Mantila L., Wischmeier M., Müller H.W., Potzel S., Coster D.P., Bonnin X. and Conway G.D. 2012 *Nucl. Fusion* **52** 103006
[6] Aho-Mantila L. *et al* 2017 *Plasma Phys. Control. Fusion* **59** 035003
[7] Rognlien T.D. *et al* 2017 *Nucl. Mater. Energy* **12** 44–50
[8] Jaervinen A.E. *et al* 2020 *Nucl. Fusion* **60** 056021
[9] Giroud C. *et al* 2015 *Plasma Phys. Control. Fusion* **57** 035004
[10] Kallenbach A. *et al* 2015 *Nucl. Fusion* **55** 053026
[11] Reimold F., Wischmeier M., Bernert M., Potzel S., Kallenbach A., Müller H.W., Sieglin B. and Stroth U. 2015 *Nucl. Fusion* **55** 033004
[12] Huber A. *et al* 2014 *Proc. 41st EPS Conf. Plasma Physics* (Berlin, Germany, 23–27 June) (http://ocs.ciemat.es/EPS2014PAP/pdf/P1.031.pdf)
[13] Glöggler S. *et al* 2019 *Nucl. Fusion* **59** 126031
[14] Bernert M. *et al* 2017 *Nucl. Mater. Energy* **12** 111–8
[15] Bernert M. *et al* 2020 *Nucl. Fusion* **61** 024001
[16] Reimerdes H. *et al* 2020 *Nucl. Fusion* **60** 066030
[17] Militello F. *et al* 2021 *Nucl. Mater. Energy* **26** 100908
[18] Subba F., Coster D.P., Escat Juanes A.N., Fable E., Wenninger R. and Zanino R. 2018 *Contrib. Plasma Phys.* **58** 758–64
[19] Subba F., Coster D.P., Moscheni M. and Siccinio M. 2021 *Nucl. Fusion* **61** 106013
[20] Subba F., Aho-Mantila L., Ambrosino R., Coster D.P., Pericoli-Ridolfini V., Uccello A. and Zanino R. 2017 *Nucl. Mater. Energy* **12** 967–72
[21] Aho-Mantila L. *et al* 2021 *Nucl. Mater. Energy* **26** 100886
[22] Xiang L. *et al* 2021 *Nucl. Fusion* **61** 076007
[23] Bonnin X. and Coster D.P. 2011 *J. Nucl. Mater.* **415** S488–91
[24] Wenninger R. *et al* 2017 *Nucl. Fusion* **57** 046002
[25] van Rooij G.J. *et al* 2013 *J. Nucl. Mater.* **438** S42–7
[26] Eich T., Sieglin B., Scarabosio A., Fundamenski W., Goldston R.J. and Herrmann A. 2011 *Phys. Rev. Lett.* **107** 215001
[27] Coster D.P., Bonnin X., Braams B., Reiter D. and Schneider R. (The ASDEX Upgrade Team) 2004 *Phys. Scr.* **T108** 7–13
[28] Dux R., Cavedon M., Kallenbach A., McDermott R.M. and Vogel G. (The ASDEX Upgrade Team) 2020 *Nucl. Fusion* **60** 126039
[29] Aho-Mantila L. *et al* 2013 *J. Nucl. Mater.* **438** S321–5
[30] Rozhansky V., Molchanov P., Veselova I., Voskoboynikov S., Kirk A. and Coster D.P. 2012 *Nucl. Fusion* **52** 103017
[31] Aho-Mantila L., Coster D.P. and Wischmeier M. 2014 *Proc. 41st EPS Conf. Plasma Physics* (Berlin, Germany, 23–27 June) (http://ocs.ciemat.es/EPS2014PAP/pdf/O4.120.pdf)
[32] Aho-Mantila L., Bonnin X., Coster D.P., Lowry C., Wischmeier M., Brezinsek S. and Federici G. 2015 *J. Nucl. Mater.* **463** 546–50
[33] David P., Bernert M., Pütterich T., Fuchs C., Glöggler S. and Eich T. (The ASDEX Upgrade Team) 2021 *Nucl. Fusion* **61** 066025
[34] Senichenkov I.Y., Kaveeva E.G., Rozhansky V.A., Voskoboynikov S.P., Veselova I.Y., Shtyrkhunov N.V., Coster D.P. and Bonnin X. 2021 *Plasma Phys. Control. Fusion* **63** 055011
[35] Rozhansky V., Kaveeva E., Molchanov P., Veselova I., Voskoboynikov S., Coster D.P., Counsell G., Kirk A. and Lisgo S. 2009 *Nucl. Fusion* **49** 025007
[36] Rozhansky V *et al* 2021 *Nucl. Fusion* **61** 126073